Science Bulletin 64 (2019) 659–668

Contents lists available at ScienceDirect

Science Bulletin

journal homepage: www.elsevier.com/locate/scib

Science Bulletin
www.scibull.com

Article

Scalable and ultrafast epitaxial growth of single-crystal graphene wafers for electrically tunable liquid-crystal microlens arrays

Bing Deng [a], Zhaowei Xin [b], Ruiwen Xue [c], Shishu Zhang [a], Xiaozhi Xu [d], Jing Gao [e], Jilin Tang [a,e], Yue Qi [a,f], Yani Wang [a], Yan Zhao [a,f], Luzhao Sun [a,f], Huihui Wang [a], Kaihui Liu [d], Mark H. Rummeli [g,h], Lu-Tao Weng [c], Zhengtang Luo [c], Lianming Tong [a], Xinyu Zhang [b], Changsheng Xie [i], Zhongfan Liu [a,j,*], Hailin Peng [a,j,*]

[a] Center for Nanochemistry (CNC), Beijing Science and Engineering Center for Nanocarbons, Beijing National Laboratory for Molecular Sciences (BNLMS), College of Chemistry and Molecular Engineering, Peking University, Beijing 100871, China
[b] Wuhan National Laboratory for Optoelectronics, School of Automation, National Key Laboratory of Science and Technology on Multispectral Information Processing, Huazhong University of Science & Technology, Wuhan 430074, China
[c] Department of Chemical and Biological Engineering, Materials Characterization and Preparation Facility, The Hong Kong University of Science and Technology, Hong Kong 999077, China
[d] State Key Laboratory for Mesoscopic Physics, School of Physics, Peking University, Beijing 100871, China
[e] Institute of Functional Nano and Soft Materials (FUNSOM), Jiangsu Key Laboratory for Carbon-Based Functional Materials and Devices, and Joint International Research Laboratory of Carbon-Based Functional Materials and Devices, Soochow University, Suzhou 215123, China
[f] Academy for Advanced Interdisciplinary Studies, Peking University, Beijing 100871, China
[g] Key Laboratory of Advanced Carbon Materials and Wearable Energy Technologies of Jiangsu Province, College of Energy, Soochow Institute for Energy and Materials Innovations, Soochow University, Suzhou 215006, China
[h] Centre of Polymer and Carbon Materials, Polish Academy of Sciences, Zabrze 41-819, Poland
[i] Wuhan National Laboratory for Optoelectronics, Huazhong University of Science & Technology, Wuhan 430074, China
[j] Beijing Graphene Institute (BGI), Beijing 100094, China

ARTICLE INFO

Article history:
Received 17 April 2019
Received in revised form 20 April 2019
Accepted 22 April 2019
Available online 24 April 2019

Keywords:
Graphene
Ultrafast growth
CuNi(1 1 1) thin film
Single crystal wafer
Liquid crystal microlens arrays

ABSTRACT

The scalable growth of wafer-sized single-crystal graphene in an energy-efficient manner and compatible with wafer process is critical for the killer applications of graphene in high-performance electronics and optoelectronics. Here, ultrafast epitaxial growth of single-crystal graphene wafers is realized on single-crystal $Cu_{90}Ni_{10}$(1 1 1) thin films fabricated by a tailored two-step magnetron sputtering and recrystallization process. The minor nickel (Ni) content greatly enhances the catalytic activity of Cu, rendering the growth of a 4 in. single-crystal monolayer graphene wafer in 10 min on $Cu_{90}Ni_{10}$(1 1 1), 50 folds faster than graphene growth on Cu(1 1 1). Through the carbon isotope labeling experiments, graphene growth on $Cu_{90}Ni_{10}$(1 1 1) is proved to be exclusively surface-reaction dominated, which is ascribed to the Cu surface enrichment in the CuNi alloy, as indicated by element in-depth profile. One of the best benefits of our protocol is the compatibility with wafer process and excellent scalability. A pilot-scale chemical vapor deposition (CVD) system is designed and built for the mass production of single-crystal graphene wafers, with productivity of 25 pieces in one process cycle. Furthermore, we demonstrate the application of single-crystal graphene in electrically controlled liquid-crystal microlens arrays (LCMLA), which exhibit highly tunable focal lengths near 2 mm under small driving voltages. By integration of the graphene based LCMLA and a CMOS sensor, a prototype camera is proposed that is available for simultaneous light-field and light intensity imaging. The single-crystal graphene wafers could hold great promising for high-performance electronics and optoelectronics that are compatible with wafer process.

1. Introduction

Graphene shows a combination of unique properties, including ultrahigh electrical mobility, extraordinary thermal conductivity, and outstanding mechanical strength, making it attractive to various applications, such as high-performance electronics [1], photonics/optoelectronics [2], and protective coatings [3]. The controlled fabrication of large-area and high-quality graphene films has been the Achilles' Heel for those promising applications [3]. Chemical vapor deposition (CVD) is considered an efficient method of graphene production due to its excellent controllability and scalability [4–7]. However, ubiquitous structural imperfections, e.g., grain boundaries [8], point defects [9], contaminants [10], and wrinkles

* Corresponding authors.
E-mail addresses: zfliu@pku.edu.cn (Z. Liu), hlpeng@pku.edu.cn (H. Peng).

https://doi.org/10.1016/j.scib.2019.04.030
2095-9273/

[11,12], counteract the superior properties of the CVD-grown graphene samples compared to exfoliated ones [7]. The controlled growth of large-size single-crystal graphene has been a continuous pursuit in graphene community.

Both single-nucleation and multi-nucleation approaches have been employed for single-crystal graphene growth [13]. For the single-nucleation approach, reducing the nucleation density is critical and to some extent realized by passivating active sites of Cu surface [14–16], locally feeding carbon sources [17,18], self-selection of the fastest-growing domain [19], etc. Moreover, great efforts have been made to promoting the growth rate, including enhancing catalytic ability of Cu by surface oxygen [14,20], accelerating the molecular collision [20,21], using substrates with high catalytic ability [17,19]. The state-of-art sizes of single-crystal graphene vary from millimeter to decimeter with growth time from several minutes to days [14,15,17,19–25]. In contrast, the multi-nucleation approach relies on appropriate substrates enabling the epitaxial graphene domains with identical orientation, which then coalesce seamlessly into a single-crystal-like film. This has been demonstrated on substrates such as h-BN [26], Ge(1 1 0) [27,28], and Cu(1 1 1) [29–32]. In comparison, the multi-nuclear approach permits abundant growth frontiers; hence, the growth rate is much faster, meaningful for the scalable and efficient production of graphene.

Very recently, the epitaxial growth of graphene on a Cu(1 1 1) substrate has received much attention, especially due to the large-size single-crystal Cu(1 1 1) foil is available by methods including temperature-driven annealing technique [32] and colossal grain growth [33]. However, there are still some problems remaining to be solved. First, the graphene orientation has not been totally controlled, with minor misorientation angles varying from 0° to 30° [30,34–36]. This deviation was ascribed to the growth temperature [36], Cu surface roughness [37], and surface impurity [30]. Second, the growth rate of graphene on Cu(1 1 1) substrates is relatively slow, because Cu(1 1 1) is a crystal face with low catalytic ability for hydrocarbon decomposition [38]. Third, the Cu(1 1 1) foil as a growth substrate is not compatible with wafer technology, which is detrimental to the integration of graphene with wafer process. Hence, designing a substrate with higher catalytic ability, better surface state (purity, cleanness, flatness, etc.) [39], and compatible with wafer processing is significant for the scalable production of single-crystal graphene and its application in electronics and optoelectronics.

Herein, we report the ultrafast epitaxial growth of single-crystal graphene on $Cu_{90}Ni_{10}$(1 1 1) thin films. Wafer-scale single-crystal $Cu_{90}Ni_{10}$(1 1 1) thin films on sapphire are fabricated by a tailored two-step sputtering process. The $Cu_{90}Ni_{10}$(1 1 1) thin film is ultrapure and ultraflat, contributing to the growth of highly-oriented graphene. The growth rate of graphene on $Cu_{90}Ni_{10}$(1 1 1) is ~50 times larger than that on Cu(1 1 1), enabling the 4 in. single-crystal graphene growth within 10 min. We designed a pilot-scale CVD system that is suitable for the scalable growth of single-crystal graphene wafers up to 25 pieces in a process cycle. The mass produced graphene wafers show good uniformity. Moreover, we demonstrate the application of single-crystal graphene in liquid-crystal microlens arrays (LCMLA) with simplified device structure, where graphene is functioned as both the transparent electrode and alignment layer. The graphene base LCMLA exhibits highly tunable focal lengths up to 2 mm under small driving voltages.

2. Experimental

2.1. Fabrication of single-crystal CuNi(1 1 1) thin film

Single-crystal sapphires (4 in., c-plane with miscut <0.5°, 600 μm thickness, epi-ready with average roughness of R_a < 0.2 nm) were used. Before deposition, the sapphire substrate was annealed at 1,050 °C for 4 h in pure oxygen atmosphere. For the two-step method to fabricate the twin-free single-crystal CuNi(1 1 1) thin film, the Cu thin film was firstly deposited on sapphire substrate by radio frequency (RF) sputtering technique using a physical vapor deposition (PVD) equipment (Sputter film, SF2). A RF power of 500 W was applied to deposit Cu thin film at the deposition rate of 0.2 nm s^{-1}, with the basal pressure of 5.32×10^{-2} Pa. A ~450 nm-thick Cu thin film was obtained after 30 min deposition. The Cu/sapphire was then annealed at 1,000 °C with 500 sccm Ar and 10 sccm H_2 at AP using a tube furnace (Thermal Scientific) for 1 h to increase the crystallinity of Cu thin film. Then, a 50 nm-thick Ni thin film was deposited on the single-crystal Cu(1 1 1)/sapphire. The Ni/Cu(1 1 1)/sapphire was alloyed at 1,000 °C with 500 sccm Ar and 10 sccm H_2 at AP for 1 h. For the one-step sputtering method, Cu thin film and Ni thin film were subsequently deposited onto the sapphire substrate in one batch to form the Ni/Cu/sapphire layered structure. Then, the same annealing process was carried out to increase the crystallinity.

2.2. Growth of graphene

For growth of single-crystal graphene, the CuNi(1 1 1) thin film was heated to 1,000 °C with 500 sccm Ar and 10 sccm H_2 at AP, then 10 sccm CH_4 (0.1% diluted in Ar) was introduced for graphene growth. The graphene grown on Cu(1 1 1) thin film was under the same condition. After growth, CH_4 gas flow was switched off and the sample was cooling down to room temperature. For the isotope labeling experiments, $^{13}CH_4$ (0.1% diluted in Ar) and $^{12}CH_4$ (0.1% diluted in Ar) were used.

2.3. Transfer of graphene

A thin film of poly(methyl methacrylate) (PMMA, 4 wt% in anisole, 2,000 r min^{-1} for 1 min) was spin-coated onto the graphene/CuNi(1 1 1). The etching of CuNi(1 1 1) is somewhat time consuming, and it usually takes 1 d to finish the etching. Then, the PMMA/graphene/CuNi(1 1 1) thin film was put into a 1 mol/L ammonium persulfate ($(NH_4)_2S_2O_8$) aqueous solution. After etching, the PMMA/graphene was rinsed in DI water for several times. The PMMA/graphene was dried in a desiccator, and then placed on the SiO_2/Si substrate. The PMMA layer was dissolved by hot acetone.

2.4. Characterization

2.4.1. Optical measurement

Bright-field and dark-field optical microscopy (OM) were conducted on Nikon, Olympus LV100ND. To measure the Raman spectra of graphene transferred onto SiO_2/Si substrate, a Witec Raman system (alpha RSA300+) with 488 nm laser was used with laser spot size of 1 μm. The spatial resolution is 500 nm and the step size is 320 nm. A 100× objective and a 600 lines/mm grating (spectral resolution was about 3 cm^{-1}) were used to collect Raman signals. WLI was conducted using a Nikon White Light Interferometry (BW-M7000).

2.4.2. UV-Ozone oxidation

Graphene/CuNi(1 1 1) thin film and graphene/Cu foil were placed into the chamber of a UV ozone cleaner (NOVASCAN PSD-UV4) equipped with a low-pressure Hg lamp. Humidity was controlled to about 40% by introducing water vapor via a water bubbler. The graphene samples were irradiated with ultraviolet light for 10 min and observed using an OM to visualize the grain boundaries.

2.4.3. XRD characterization

A Panalytical X-pert system (Materials Research Diffractometer) with Cu Kα radiation source was employed. Different geometrical set-ups of the instrument were used depending on scanning procedure. Monochromator and Ni 0.125 mm automatic beam attenuator and a 0.18° parallel plate collimator diffracted optics were used. The high resolution mode enables the angle resolution of 0.001°.

2.4.4. SEM and EBSD measurement

Scanning electron microscopy (SEM) images were obtained on a Hitachi S4800 field-emission scanning electron microscope. Electron backscatter diffraction (EBSD) measurements were carried out on ULVAC-PHI (PHI 710) Auger system equipped with the EBSD probe (EDAX, DigView). EBSD test was operated at 10 kV voltage and 10 nA current. The spot size was 20 nm and the angular resolution was of the order of 0.1°, which allow the quantification of the misorientation between subgrains or twins and its correlation with the local microstructure.

2.4.5. AFM measurement

Atomic force microscopy (AFM) morphology image was carried out on a Bruker Dimension Icon with a Nanoscope V controller using the tapping mode.

2.4.6. LEED measurement

Low energy electron diffraction (LEED) was performed using Omicron LEED system in ultrahigh vacuum with base pressure below 3×10^{-7} Pa.

2.4.7. TEM measurement

Graphene was transferred onto an Au grid using the polymer-free transfer method. The high-resolution TEM (HRTEM) and selected area electron diffraction (SAED) were performed on an FEI Titan cubed with a Cs corrector for the objective lens. The electron acceleration voltage was 80 kV.

2.4.8. XPS measurement

X-ray photoelectron spectroscopy (XPS) was conducted on the XPS Kratos Axis Ultra-DLD spectrophotometer with monochromatic Al X-ray at pressure of 5×10^{-9} to 1×10^{-8} Torr.

2.4.9. ToF-SIMS analysis

Time-of-flight secondary ion mass spectrometry (ToF-SIMS) measurements were carried out with a TOF-SIMS V (ION-TOF GmbH, Munster, Germany) instrument. A bismuth liquid-metal ion source and a Cs^+ ion beam were equipped for analysis and sputtering, respectively. A 3 keV-Cs^+ beam scanning over typically an area of 350 μm × 350 μm with a current of 30 nA was used to sputter through the CuNi(1 1 1) or graphene/CuNi(1 1 1). Ion images were taken using 25 keV-Bi^+ primary ion over an area of 100 μm × 100 μm at the center of Cs sputtering with 128 × 128 raster pixel sizes. The whole depth profiling process was run in the interlaced mode, consisting of cycles of short pulses of Bi^+ followed by a long period of Cs^+ sputtering. The vacuum during the analysis was about 1.5×10^{-9} mbar.

2.5. Fabrication of the single-crystal graphene LCMLA (SCGLCMLA) device

Single-crystal graphene was transferred onto 500-μm-thick silica substrates as the bottom electrode. A hole-patterned indium tin oxide (ITO) coated silica was used as the top electrode. The pattern shape in the electrode is an array of circular holes with a diameters of 128 μm and a center-to-center space of 160 μm, which was fabricated by photolithography and wet etching. The graphene silica is adhered to the hole-patterned ITO silica using an adhesive along the device edges. The adhesive was mixed with a number of glass microspheres with 20-μm diameters to form an inner microcavity. Then, the microcavities were fully filled with twisted nematic LC materials (Merck E44: $n_o = 1.5277$ and $n_e = 1.7904$). Finally, the device was interconnected using conductive paints and tapes.

2.6. Focusing and imaging test of the SCGLCMLA device

The focusing characters and point spread functions (PSFs) were acquired by a beam analyzer of WinCamD of DataRay, Inc. The collimated beams emitting from the laser source (central wavelength: 671 nm, Changchun New Industries Optoelectronics Tech. Co., Ltd.) were normalized to the sample through a polarizer working in the visible regime. Converging patterns were collected using a microscope objective of ×40 and 0.65 numerical aperture on a Laser Beam Profiler coupled to the SCGLCMLA. The SCGLCMLA device was driven by a tunable AC voltage signal of 1 kHz square wave. To test the imaging capability, the SCGLCMLA was integrated on the CMOS sensor of MVC14KSAC-GE6-NOO of Microview, using a main lens (M3520-MPW2) with focal length of 35 mm. The size of CMOS sensor is 4384 × 3288 with a pixel pitch of 1.4 μm. The intensity and light field images were obtained by adjusting the driving voltages applied on the SCGLCMLA.

3. Results and discussion

Several groups have reported the hetero-epitaxy of (1 1 1)-oriented CuNi thin films on α-Al_2O_3(0001) (sapphire) substrates [35,40,41]. However, similar to the case of Cu epitaxy on sapphire [36,42–44], dense in-plane twin structures and grooves in the CuNi thin films are difficult to eliminate and degrade the surface flatness. Here, a two-step magnetron sputtering approach is proposed to essentially prevent the twin formation in $Cu_{90}Ni_{10}$(1 1 1) thin films (Fig. 1a). In the first step, the single-crystal Cu(1 1 1) thin film with least twin structures was fabricated on sapphire according to the method we described before [45]. Briefly, the sapphire substrate was firstly annealed in oxygen to release the inner stress accumulated during the manufacturing process, and to optimize the surface termination. A 450-nm Cu film was then deposited onto sapphire by magnetron sputtering. Single-crystal Cu(1 1 1) thin films without twin were obtained after high-temperature recrystallization (Fig. S1a–c online). In the second step, 50-nm Ni was deposited on the Cu(1 1 1)/sapphire (Fig. S1d–f online). The as-deposited Ni is with twins due to the different stack of Ni of Cu, that is ABC stack and ACB stack, is energetically the same (Fig. 1a, inset). In the third step, the Ni/Cu(1 1 1) was annealed in Ar/H_2 at high temperature, where the Ni domains with 60° misorientations diffused into the single-crystal Cu(1 1 1) matrix and register with the Cu(1 1 1) to form the single-crystal $Cu_{90}Ni_{10}$(1 1 1) alloy.

Fig. 1b shows a wafer-scale $Cu_{90}Ni_{10}$ film with mirror-like surface. The surface is very flat with root-mean-square (RMS) roughness of ~0.50 nm in the image region of 25 μm^2, as characterized by AFM (Fig. 1c). According to the optical profile measured by white light interferometry (WLI), the surface flatness of CuNi film in a large area is much better than that of Cu film (Fig. S2 online), which can be ascribed to the inhibited sublimation due to the minor content of Ni. Note that CuNi(1 1 1) thin film is much more flat than Cu(1 1 1) foils with high-density and rough rolling lines formed during the manufacturing process [30,46].

EBSD and X-ray diffraction (XRD) were carried out to investigate the polar and azimuthal mosaicity of the CuNi thin film. The uniform blue contrast of the EBSD image proves that the out-of-plane orientation is (1 1 1) (Fig. 1d). The pole figure (inset in

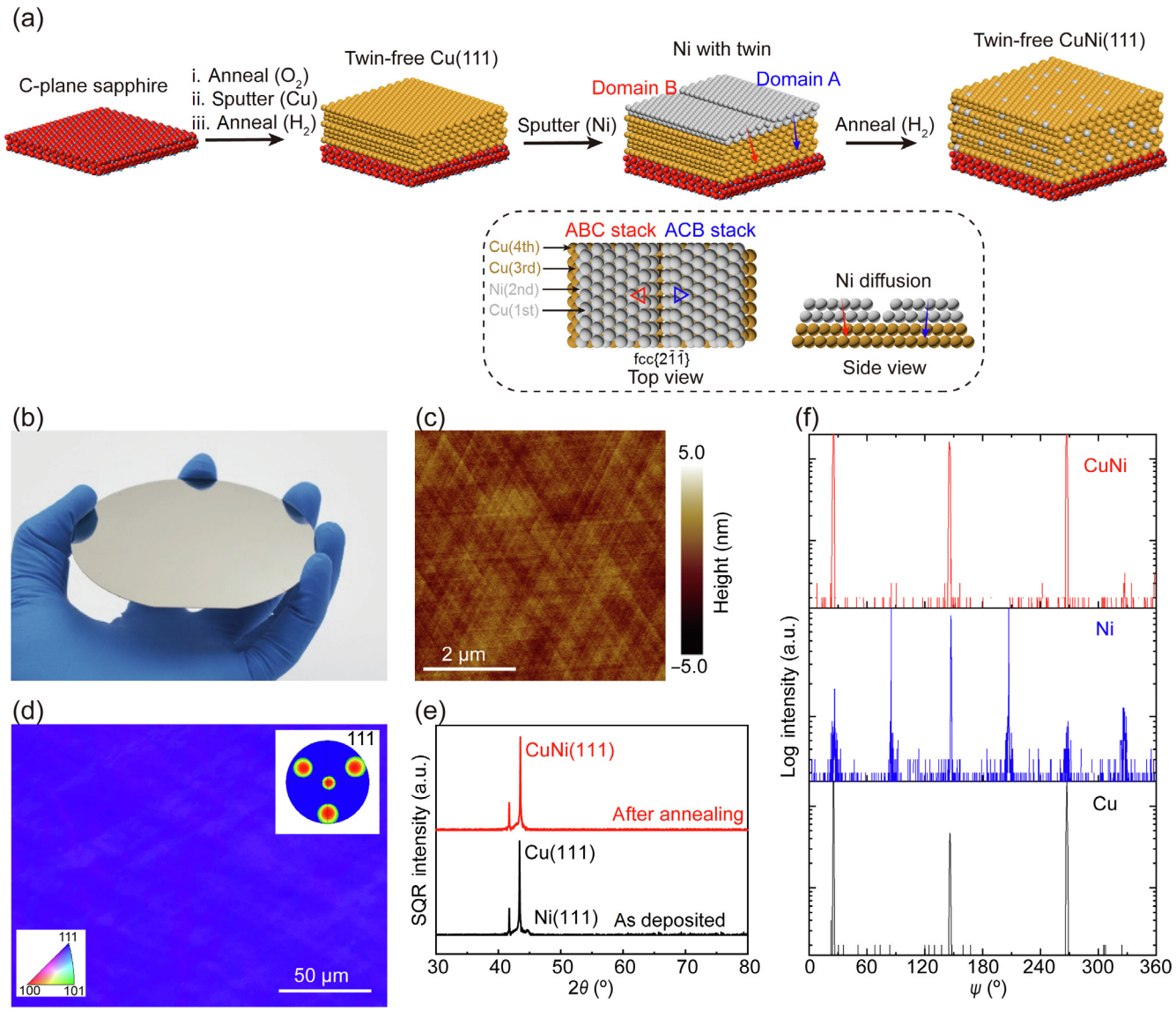

Fig. 1. Fabrication of single-crystal $Cu_{90}Ni_{10}$(1 1 1) thin films. (a) Schematic of the two-step sputtering method. Inset shows the top view and side view of the Ni with twin boundary. (b) Photograph of a 4 in. CuNi(1 1 1) thin film on sapphire. (c) AFM image of the CuNi(1 1 1) thin film. (d) EBSD image of the CuNi(1 1 1) thin film. Inset shows the pole figure of the same region. (e) XRD patterns of as-deposited Ni/Cu(1 1 1)/sapphire and CuNi(1 1 1)/sapphire after alloying. (f) ψ scan of Cu(1 1 1), Ni/Cu(1 1 1), and CuNi (1 1 1) thin films.

Fig. 1d) shows three evenly distributed points, indicating the single azimuthal orientation without in-plane twinning. XRD was then used to track the evolution of mosaicity in a large area. The $\theta/2\theta$ scan shows that the as-deposited Ni on Cu(1 1 1)/sapphire is (1 1 1)-dominated (Fig. 1e). After annealing, only one peak is present between the peak positions of Cu(1 1 1) and Ni(1 1 1), indicating the formation of CuNi(1 1 1) alloy. We then chose M(2 0 0) (M = Cu, Ni, $Cu_{90}Ni_{10}$) and Al_2O_3(02–24) as Bragg positions and performed an azimuthal scan (φ) by rotating the sample normal to surface using high-resolution XRD (HRXRD). As shown in Fig. 1f, three diffraction peaks at the interval of 120° appear for the Cu (1 1 1) thin film, while the as-deposited Ni thin film showed six peaks at the interval of 60°, indicating the existence of the in-plane twin structures in as-deposited Ni film. Remarkably, after annealing, the CuNi(1 1 1) film exhibits three evenly distributed peaks with narrow full width at half-maximum (fwhm). All those observations prove the excellent single crystalline nature of the CuNi(1 1 1) thin film.

The tailored two-step magnetron sputtering approach is the key to fabricate the high-quality single-crystal CuNi(1 1 1) thin films. In the controlled experiment, one-step sputtering approach was employed to deposit the CuNi thin films [40]. Cu and Ni layers were subsequently deposited onto the sapphire substrates, followed by annealing at high temperature to form the alloy (Fig. S3a online). The morphology characterized by SEM and AFM shows abundant grain boundaries with deep thermal grooves (Fig. S3b–d online). HRXRD and EBSD also proved the ubiquitous twin structures in the CuNi(1 1 1) thin film fabricated by the one-step sputtering approach (Fig. S3e–g online).

Graphene was grown on the $Cu_{90}Ni_{10}$(1 1 1) thin film using atmospheric pressure CVD (APCVD). The graphene domains grown on $Cu_{90}Ni_{10}$(1 1 1) thin films were hexagonal and well aligned (Figs. 2a and S4 (online)), which then coalesced into a continuous monolayer by elongating the growth time (Fig. 2a). Graphene was also grown on Cu(1 1 1) thin films under the same conditions (Fig. S5 online). The growth of fully covered graphene on a 4 in. CuNi(1 1 1) costs only 10 min, corresponding to the growth rate of 1 cm/min, 10 times faster than that of Cu(1 1 1) (Fig. 2b). In addition, the growth rate of a single domain on CuNi(1 1 1) thin films reaches 50 μm/min, comparable with previous reported

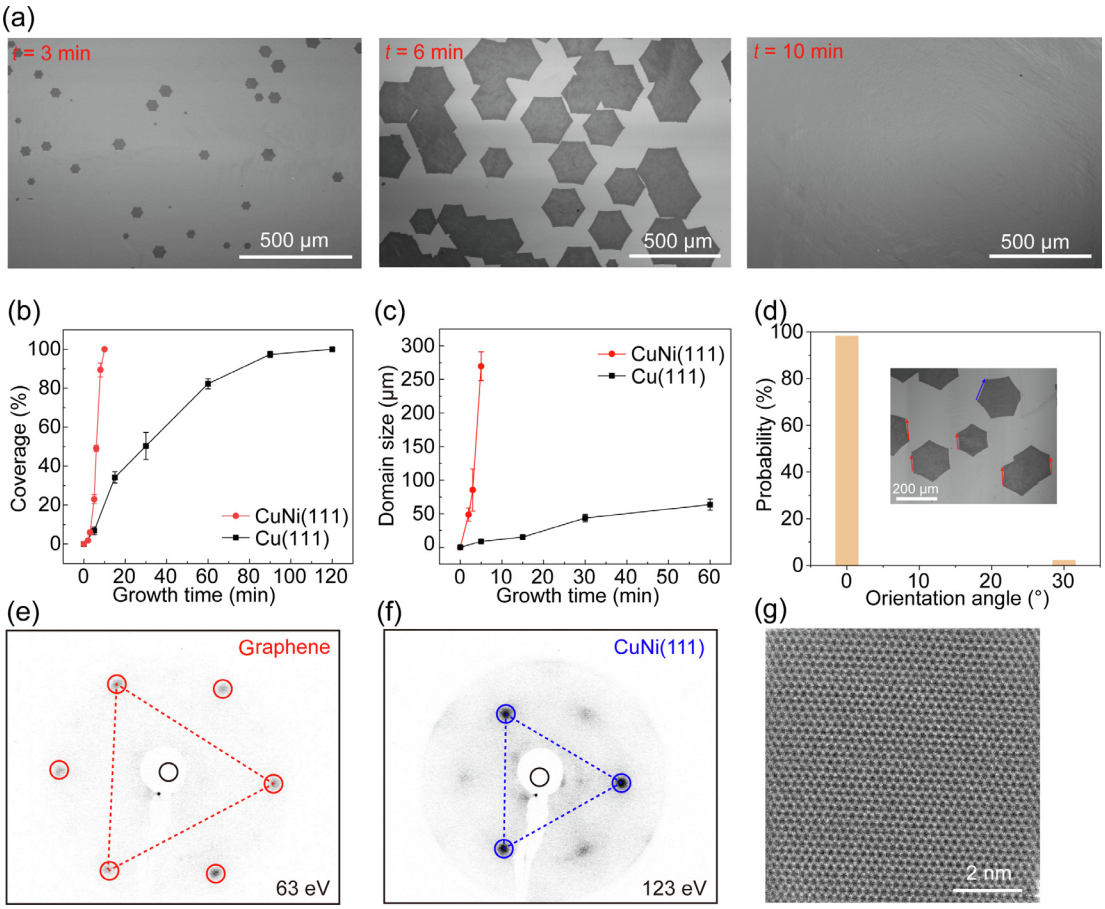

Fig. 2. Ultrafast epitaxial growth of single-crystal graphene wafer on $Cu_{90}Ni_{10}$(1 1 1). (a) SEM images of graphene grown on CuNi(1 1 1) with different growth time. (b) Coverage of graphene grown on Cu(1 1 1) and CuNi(1 1 1). (c) Domain size of graphene grown on Cu(1 1 1) and CuNi(1 1 1). (d) Statistic of orientation distribution of graphene grown on CuNi(1 1 1). Inset is a SEM image of graphene with 0° (red arrow) and 30° (blue arrow) orientation. (e,f) LEED patterns of graphene grown on CuNi(1 1 1). LEED pattern of graphene (e) under lower electron energy. LEED pattern of CuNi(1 1 1) (f) under higher electron energy. (g) Atomic-resolution HRTEM image of graphene.

values on a CuNi foil [17,47], and 50 times larger than that on Cu(1 1 1) thin film (~1 μm/min) (Fig. 2c). The difference in growth rate between coverage and single domain originates from the reduced nucleation density of graphene on the CuNi(1 1 1) alloy [47].

Multi-scale characterizations were conducted to verify the orientation of graphene grown on CuNi(1 1 1). First, we checked the orientation of graphene domains using SEM based on the common view that graphene domains are terminated by zigzag edge under high H_2/CH_4 ration (=1,000:1 in our experimental condition). The percentage of aligned graphene domains is larger than 98% (Fig. 2d) according to over 1000 graphene domains. The remaining domains have the misorientation angle of exclusively ~30°, consistent with theoretical calculation that the orientation angle of 30° with regards to Cu[1 1 0] is the second stable state on Cu(1 1 1) [48]. It is worth noting that no other misorientation angles was observed. The high purity and high surface flatness of CuNi(1 1 1) may contribute to preventing the random nucleation usually present in Cu(1 1 1) or CuNi(1 1 1) foils [30]. In addition, the twin boundaries of CuNi(1 1 1) (made by one-step sputtering method) can degenerate the orientation and shape of graphene domains (Fig. S6 online). Then, LEED was used to characterize the lattice structure and orientation of graphene/CuNi(1 1 1). Only one pattern was observed for the graphene layer, indicating the single crystalline nature (Fig. 2e). Moreover, the LEED pattern of graphene are of the same direction with underlying $Cu_{90}Ni_{10}$(1 1 1) (Fig. 2f), demonstrating the epitaxial graphene growth. Furthermore, we transferred the continuous graphene film onto TEM grids and carried out TEM and SAED characterization. Over 50 diffraction patterns were randomly collected on graphene transferred onto a TEM grid (with diameter of ~3 mm), which were exactly identical (Fig. S7 online).

The stitching of multiple graphene islands grown on CuNi(1 1 1) were investigated in detail. Graphene grain boundaries can be directly visualized using OM imaging after exposure to UV irradiation [49]. Grain boundary lines were clearly present at the stitching regions of two misaligned graphene islands grown on polycrystalline Cu foils; in contrast, the graphene/CuNi(1 1 1) withstand the harsh environment and showed no obvious contrast (Fig. S8 online). Raman spectroscopy was employed to identify defects in graphene lattice. The I_D/I_G map showed no defect at the stitching frontier of two aligned graphene islands (Fig. S9a online). The I_{2D}/I_G band ratio was ~4 and uniform across the two domains. Both indicated the single-crystal and monolayer feature of graphene. As a comparison, a defect line can be visualized at the stitching region of misaligned graphene domains (Fig. S9b online) [50]. The seamless stitching of graphene domains grown on CuNi(1 1 1) was further confirmed by HRTEM (Fig. S10 online). The atomic-resolution image shows the perfect hexagonal lattice of monolayer graphene, demonstrating its high quality and free of defect (Fig. 2g).

The strict monolayer (without any adlayer) and ultrafast growth features inspire us to explore the growth mechanism of graphene on $Cu_{90}Ni_{10}$(1 1 1) thin films. As we know, the growth of graphene obeys the surface-reaction mediated regime on Cu

and the segregation regime on Ni. To clarify the growth mechanism of graphene on $Cu_{90}Ni_{10}$(1 1 1), carbon isotope labeling experiments were performed. Raman spectroscopy was used to visualize the carbon supply, where the Raman 2D band at ~2,700 cm^{-1} represents the signal from ^{12}C-derived graphene, while ~2,600 cm^{-1} from ^{13}C-derived graphene (Fig. S11 online) [51]. $^{12}CH_4$ was first introduced to initiate the nucleation and growth of graphene for 1 min; then, carbon source was switched to $^{13}CH_4$ for the other 1 min, followed by fast moving growth substrate out to cold zone of CVD system to break off the growth. For comparison, similar procedure was applied to the graphene growth on Cu(1 1 1) with subsequent supply of $^{12}CH_4$ and $^{13}CH_4$ for both 15 min. Graphene films were transferred onto SiO_2/Si substrates where Raman map was conducted (Fig. 3a, b). The shape of graphene grown on Cu (1 1 1) is more compact and regular than that on CuNi(1 1 1), which can be ascribed to the different growth regime of graphene on Cu(1 1 1) and CuNi(1 1 1). The growth rate of graphene on CuNi (1 1 1) is much faster than that on Cu(1 1 1). Hence, the graphene growth on Cu(1 1 1) is attachment-limited, and graphene growth o CuNi(1 1 1) is diffusion-limited. For graphene synthesized on CuNi(1 1 1), the transition from pure ^{12}C to ^{13}C region was very sharp, identical to that of graphene synthesized on Cu(1 1 1) (Fig. 3c). Moreover, the Raman spectrum at the transition region showed the coexistence of two pure bands from ^{13}C and ^{12}C (Fig. 3d), clearly confirming no mixture of ^{13}C and ^{12}C during growth (inset in Fig. 3d). Hence, we conclude that graphene grown on $Cu_{90}Ni_{10}$(1 1 1) thin films is surface-reaction dominated and without segregation [17].

To interrupt the growth regime, XPS was conducted to investigate the surface element distribution of the CuNi alloy. Element depth profile of the CuNi thin film shows that the content of Ni and Cu were constant in the bulk, while Cu enrichment on the surface was observed (Fig. S12 online). Specifically, the surface concentration of Ni was ~6%, while the bulk content was ~10%. This phenomenon may be ascribed to the Cu surface segregation since Cu has a lower heat of sublimation than Ni [52]. The low concentration of Ni on the surface accounts for the surface-reaction mediated growth [17]. More importantly, we found that the elements ratio (both in-bulk and on-surface) did not vary with annealing time at high temperature (Fig. S13 online), which is meaningful for the reuse of CuNi(1 1 1) substrate.

In order to further investigate the C distribution of CuNi(1 1 1) after graphene growth, ToF-SIMS was conducted owing to its excellent sensitivity and atomic layer resolution in depth [17]. Before graphene growth, C concentration is negligible (Fig. S14a–c online). After the fully covered graphene growth, the depth pro-

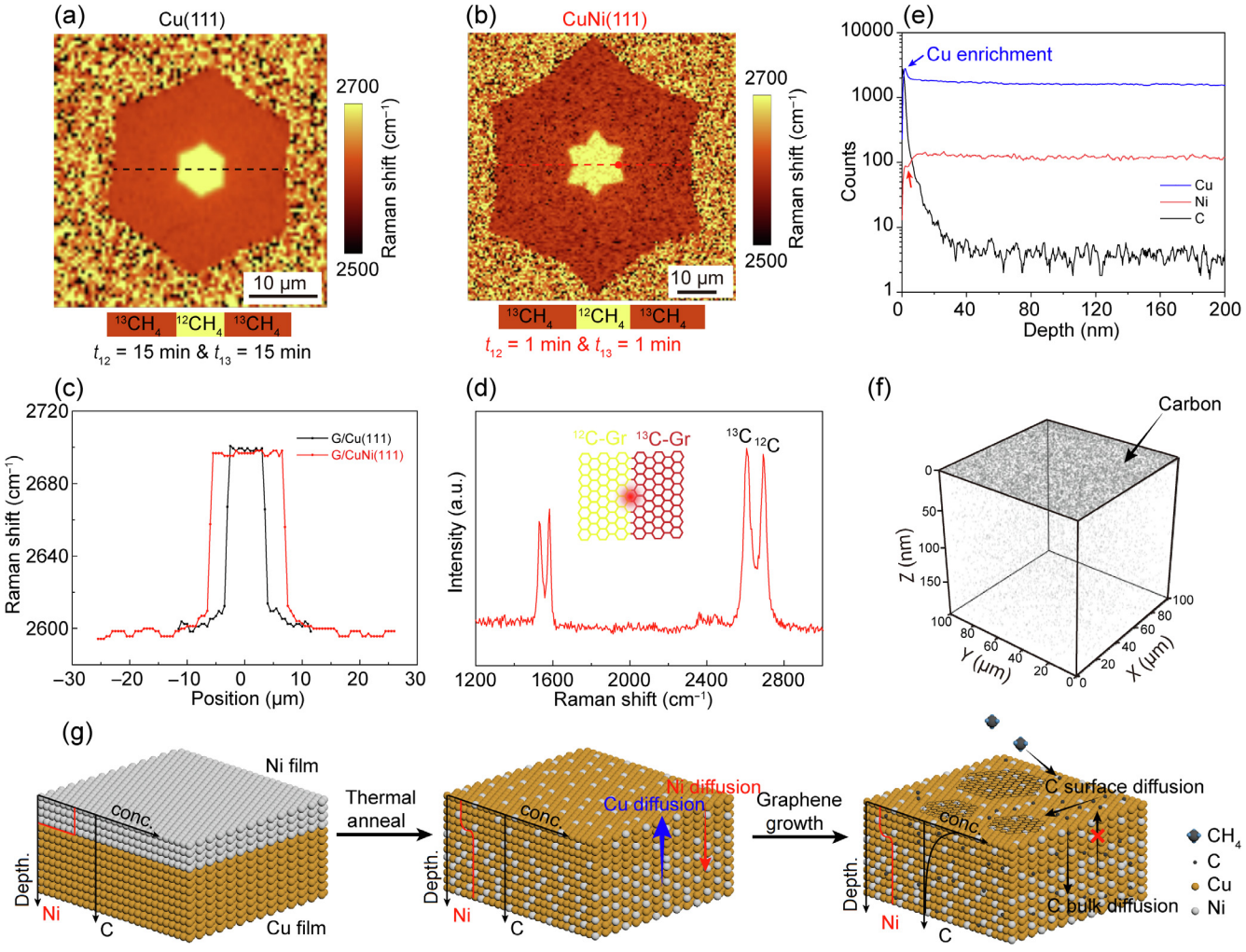

Fig. 3. Mechanism of graphene growth on $Cu_{90}Ni_{10}$(1 1 1) thin film. (a) Raman 2D band position map of a graphene domain grown on Cu(1 1 1). (b) Raman 2D band position map of a graphene domain grown on CuNi(1 1 1). (c) 2D band position profile of graphene grown on Cu(1 1 1) along the black line in (a) and CuNi(1 1 1) along the red line in (b). (d) Raman spectrum of the red point in (b). Inset shows the sharp boundary of ^{12}C-graphene and ^{13}-graphene. (e) In-depth element distribution of graphene/CuNi(1 1 1) measured by ToF-SIMS. (f) 3D carbon element map of graphene/CuNi(1 1 1). (g) Proposed growth mechanism of graphene on $Cu_{90}Ni_{10}$(1 1 1).

files of Cu, Ni, and C were collected (Figs. 3e and S14d, f (online)). The peak of Cu and the valley of Ni near the surface also proved the Cu enrichment on the surface of the CuNi alloy. The C concentration drop rapidly from surface to bulk, indicating that the C concentration was far from thermal equilibrium and not saturated in the bulk. The 3D carbon map of the graphene/CuNi showed that the signals concentrated on the surface, which were derived from the graphene monolayer (Fig. 3f).

Based on these observation, we proposed the growth mechanism of graphene on CuNi(1 1 1), as schematically shown in Fig. 3g. The carbon concentration (conc.) is negligible on the as deposited Ni/Cu(1 1 1). During annealing, the Cu diffusion exceeds the Ni diffusion, resulting in the surface enrichment of Cu. Ni accelerates the decomposition of methane on the surface of CuNi alloy to form carbon radicals. Some reactive carbon radicals diffuse on the surface to initiate the nucleation and growth of graphene. Some carbon radicals diffuse into the bulk of CuNi alloy since the Ni has relatively high carbon solubility. However, the diffusion of bulk carbon onto the surface is blocked because the surface is Cu rich. Hence, the graphene grown on the $Cu_{90}Ni_{10}$(1 1 1) obeys the surface reaction regime and is an exact monolayer.

One of the major benefits of the growth of single-crystal graphene wafers on CuNi(1 1 1) thin films is the compatibility with wafer process. Here, we designed and built a pilot-scale APCVD system for scalable growth of the graphene wafers (Fig. 4a). The highly automatically controlled furnace is mainly composed of a resistance heating unit (heater), a sealed chamber (SiC tube with diameter of 30 cm), and a quartz stage for loading CuNi wafers. 25 pieces of 4 in. CuNi wafers were loaded for graphene growth in a process cycle (Fig. 4b). Recent experiment [53] and theoretical calculation [54] suggest that gas-phase dynamics plays an important role in graphene growth, including the uniformity, thickness, and growth rate. For the mass production of graphene, uniform gas flow and thermal field are of special significance. To improve the uniformity of gas flow, the CVD chamber is designed with multiple gas inlet nozzles with diameter of ~1 cm, and the distance

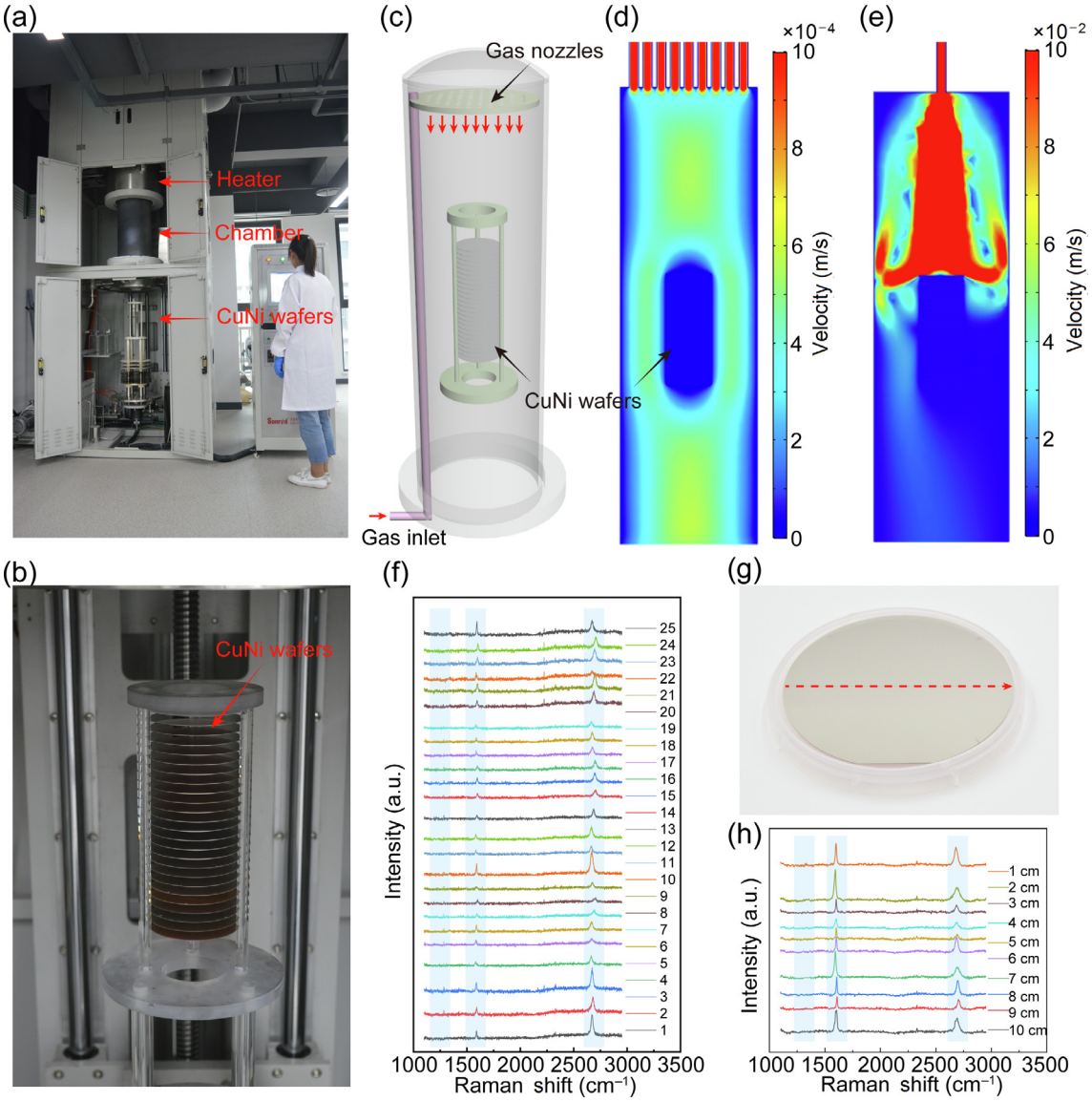

Fig. 4. Scalable growth of single-crystal graphene wafers. (a) A pilot-scale APCVD furnace for scalable growth of single-crystal graphene wafers on CuNi(1 1 1). (b) 25 pieces of CuNi(1 1 1) wafer for graphene growth in a process cycle. (c) Scheme of the gas flow and architecture of CuNi wafers inside the chamber. Simulation of the gas flow velocity distribution with multiple gas nozzles (d) and single gas nozzle (e). (f) Raman spectra of graphene grown on 25 pieces of CuNi(1 1 1) wafers in a process cycle. (g) Photograph of a graphene/CuNi(1 1 1) wafer. (h) Raman spectra of graphene grown on a CuNi(1 1 1) wafer at varied positions in (g).

between the CuNi wafers is ~1 cm, as schematically shown in Fig. 4c. We then performed a computational fluid dynamic simulation on gas-dynamics of the vertical CVD chamber based on finite element method (FEM). In the case of multiple gas inlet nozzles, the velocity of gas flow becomes uniform quickly and keeps stable across the whole chamber (Fig. 4d). In striking contrast, in the case of single gas-inlet hole, the gas flow is turbulent and nonuniform above and below the wafers, which would hinder the stable growth of graphene (Fig. 4e).

We then carefully optimized the growth condition of single-crystal graphene on CuNi(1 1 1) wafers using the pilot-scale equipment, including gas flow, gas ratio, temperature, etc. The quality and uniformity of graphene within a wafer and among the 25 wafers were evaluated. The Raman spectra of single-crystal graphene films grown on 25 pieces of CuNi(1 1 1) wafers in a process cycle were shown in Fig. 4f. No obvious D peak is visualized for all the graphene wafers, indicating the high quality. We then characterized the quality of graphene along the diameter of a single-crystal graphene wafer grown on CuNi(1 1 1) (Fig. 4g, h). There is also no observation of any defect peak, demonstrating the high uniformity among the whole wafer. Single-crystal graphene wafers were also transferred onto SiO_2/Si substrates. The optical microscopy (OM) images and Raman spectra of graphene along the diameter of a wafer and among 25 pieces of wafers demonstrated the high-quality and uniform monolayer feature (Fig. S15 online). These observations prove that the pilot-scale CVD equipment and the optimized growth protocols exhibit decent yield rate of graphene, which is critical for quality control of scalable production.

Single-crystal graphene exhibits lots of merits compared to the polycrystalline counterpart, including higher mobility, higher conductivity, and identical lattice orientation. These properties render the single-crystal graphene wafer very promising in liquid crystal (LC) optoelectronics [55,56], considering that graphene plane can induce ordered packing of LC [30,57] and be an excellent transparent conductive layer [58,59]. Here, we demonstrated the application of single-crystal graphene in LCMLA. Microlen arrays are widely used in phenoptic camera to acquire the position and direction of irradiance of a scene by inserting the microlens arrays between the main lens and photography sensor [60,61]. Recently, the light field camera based on LCMLA with tunable focal length has been proposed to extend the depth of field and improve the functionality [62–65].

The device structure of SCGLCMLA is shown in Fig. 5a. Nematic liquid crystals were sealed into the microcavity gapped by a single-crystal graphene (SCG) coated silica and a patterned ITO coated silica. The LC layer was directly oriented by the SCG; hence, an alignment layer such as polyimide film is not necessary [63,66], which greatly simplified the device structure and fabrication process. Coupled with an imaging sensor, the SCGLCMLA can be used as a lens with electrically tunable focal length (Fig. 5b). In the on state

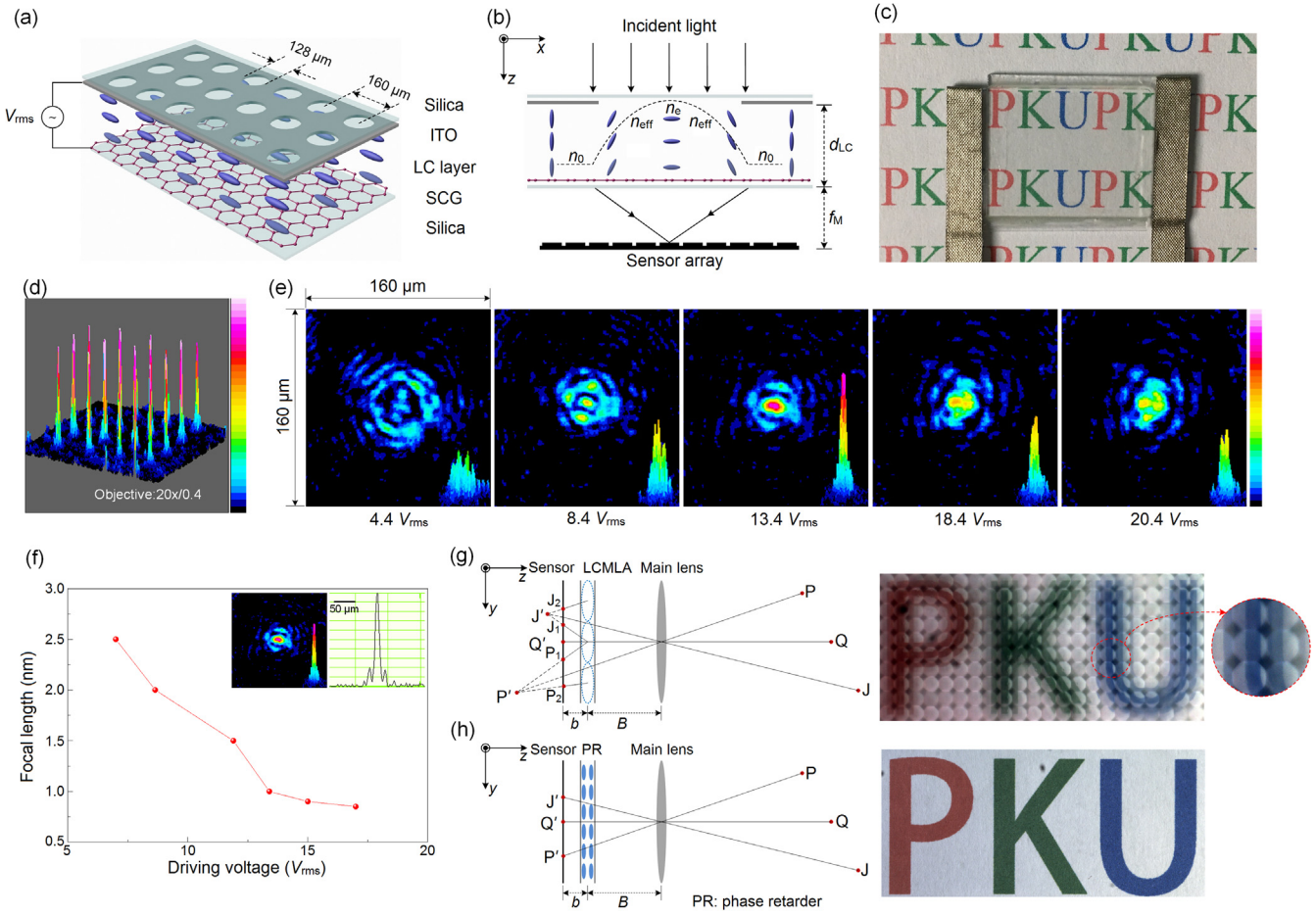

Fig. 5. Liquid-crystal microlens arrays based on single-crystal graphene wafer. (a) Schematic of the SCGLCMLA device. (b) Schematic of the SCGLCMLA device coupled with imaging sensor arrays. The black dash line indicates the equivalent reflective index distribution profile of the single microlen under a driving voltage. d_{LC}, the thickness of the LC device; f_M, the focal length; the two principle refractive indices are n_0 and n_e respectively; the refractive index for extraordinary waves is n_{eff}. (c) Photograph of the SCGLCMLA device. (d) PSFs of a number of microlens. The intensity is normalized. (e) PSFs of a microlen under different driving voltages. (f) Relationship between the focal length and the driving voltage. Inset, the focused PSF and intensity line profile of a microlen. (g) Schematic of the prototype camera working in the light field mode (left) and an acquired light field image (right). (h) Schematic of the prototype camera working in conventional mode (left) and an acquired intensity image (right).

of the SCGLCMLA, when an external voltage is applied on the LC cell, the LC molecules between two planar electrodes will be rearranged along the electric field direction; as a result, the incident light will be focused on the sensor array. In the off state, when external voltage is absence, the SCGLCMLA can be referred as a phase retarder (PR). The photograph of a SCGLCMLA device with functional area of 2 cm × 2 cm was shown in Fig. 5c. The device is highly transparent, critical to prevent the loss of light intensity.

The focusing characters and PSFs were acquired using a Standard Beam Profiling Camera (WinCamD of DataRay, Inc.). The optical measurement system for analyzing and evaluating the SCGLCMLA is shown in Fig. S16 (online). The similar PSFs of a number of microlens over a large area showed the high uniformity of the device (Fig. 5d). By varying the driving voltages, the optical patterns along the optical axis of an individual microlen were acquired (Fig. 5e). The focus is a small circular spot with a very sharp PSF at the driving voltage of 13.4 V, indicating that the focal length at the specific voltage is ~1 mm, the sum of the thickness of the silica substrate plus the distance between the SCGLCMLA and the lens of the microscope. The focal length can be continuously tuned by varying the driving voltage (Fig. 5f), ranging from ~2.5 to ~0.75 mm under a small voltage variation between ~7 and ~17 V.

Then, the imaging functionality of the SCGLCMLA was tested by a prototype camera that integrate the electro-optical device with a CMOS sensor. The significant capability of the prototype camera is that it can be used to obtain the light-field and intensity images simultaneously. When driving voltages were applied on the SCGLCMLA, a gradient refractive index that corresponded to the rearrangement of LC molecules under the microholes pattern was formed (Fig. 5g, left). In this scenario, the light field information can be remapped on the image sensor (Fig. 5g, right). Compared with the conventional camera, the depth-of-field of phenoptic camera was extended through the electrically tunable focal length. Hence, with further computation process, the digital refocusing image, perspective shift image, depth map, and three-dimensional reconstruction can be obtained. When the voltage signal applied on the SCGLCMLA was absence, SCGLCMLA represented a phase retarder and the prototype became a conventional camera (Fig. 5h, left). In this scenario, the intensity image of "PKU" can be recorded (Fig. 5h, right). The implementation of the single-crystal graphene based LCMLAs represent an excellent example for its application in optoelectronics that is compatible with CMOS technology.

4. Conclusion

In summary, for the first time, wafer-size single-crystal Cu_{90}-Ni_{10}(1 1 1) thin films were fabricated on sapphire through a tailored two-step magnetron sputtering process. Ultrafast epitaxial growth of single-crystal graphene wafers was realized on the CuNi(1 1 1) thin film, with growth rate 50 times larger than that on Cu(1 1 1). The cost-efficient and wafer process compatible growth method holds great promise for mass production of high-quality graphene films, as demonstrated by a pilot-scale CVD system for the scalable growth of single-crystal graphene wafers, which will greatly accelerate the high-end application of graphene in electronics and optoelectronics.

Conflict of interest

The authors declare that they have no conflict of interest.

Acknowledgments

We thank Drs. Jinxiong Wu, Rui Yan, and Yin Du for helpful discussion. This work was supported by the National Basic Research Program of China (2016YFA0200101 and 2014CB932500), the National Natural Science Foundation of China (21525310, 51432002, 51520105003, 61432007, and 61176052), and Beijing Municipal Science & Technology Commission (Z161100002116021 and Z181100004818001).

Author contributions

Hailin Peng and Bing Deng conceived the experiment. Hailin Peng and Zhongfan Liu supervised the project. Bing Deng conducted the synthesis and characterization with the help of Jilin Tang, Yani Wang, Yue Qi, Huihui Wang, and Luzhao Sun. The liquid-crystal devices were fabricated and measured by Zhaowei Xin, Xinyu Zhang, and Changsheng Xie. The LEED test was conducted by Xiaozhi Xu and Kaihui Liu. The Raman test was conducted by Shishu Zhang, Yan Zhao and Lianming Tong. The ToF-SIMS was conducted by Ruiwen Xue, Lu-Tao Weng and Zhengtang Luo. The TEM was conducted by Jing Gao and Mark H. Rummeli. Bing Deng and Hailin Peng wrote the paper. All the authors discussed the results and commented on the manuscript.

Appendix A. Supplementary data

Supplementary data to this article can be found online at https://doi.org/10.1016/j.scib.2019.04.030.

References

[1] Novoselov KS, Geim AK, Morozov SV, et al. Electric field effect in atomically thin carbon films. Science 2004;306:666–9.
[2] Bonaccorso F, Sun Z, Hasan T, et al. Graphene photonics and optoelectronics. Nat Photonics 2010;4:611–22.
[3] Novoselov KS, Fal'ko VI, Colombo L, et al. A roadmap for graphene. Nature 2012;490:192–200.
[4] Tetlow H, de Boer JP, Ford IJ, et al. Growth of epitaxial graphene: theory and experiment. Phys Rep 2014;542:195–295.
[5] Munoz R, Gomez-Aleixandre C. Review of CVD synthesis of graphene. Chem Vapor Depos 2013;19:297–322.
[6] Yan K, Fu L, Peng HL, et al. Designed CVD growth of graphene via process engineering. Acc Chem Res 2013;46:2263–74.
[7] Li XS, Colombo L, Ruoff RS. Synthesis of graphene films on copper foils by chemical vapor deposition. Adv Mater 2016;28:6247–52.
[8] Huang PY, Ruiz-Vargas CS, van der Zande AM, et al. Grains and grain boundaries in single-layer graphene atomic patchwork quilts. Nature 2011;469:389.
[9] Banhart F, Kotakoski J, Krasheninnikov AV. Structural defects in graphene. ACS Nano 2011;5:26–41.
[10] Lin YC, Lu CC, Yeh CH, et al. Graphene annealing: how clean can it be? Nano Lett 2012;12:414–9.
[11] Zhang Y, Gao T, Gao Y, et al. Defect-like structures of graphene on copper foils for strain relief investigated by high-resolution scanning tunneling microscopy. ACS Nano 2011;5:4014–22.
[12] Zhu WJ, Low T, Perebeinos V, et al. Structure and electronic transport in graphene wrinkles. Nano Lett 2012;12:3431–6.
[13] Nguyen VL, Lee YH. Towards wafer-scale monocrystalline graphene growth and characterization. Small 2015;11:3512–28.
[14] Hao YF, Bharathi MS, Wang L, et al. The role of surface oxygen in the growth of large single-crystal graphene on copper. Science 2013;342:720–3.
[15] Zhou HL, Yu WJ, Liu LX, et al. Chemical vapour deposition growth of large single crystals of monolayer and bilayer graphene. Nat Commun 2013;4:2096.
[16] Lin L, Li JY, Ren HY, et al. Surface engineering of copper foils for growing centimeter-sized sngle-crystalline graphene. ACS Nano 2016;10:2922–9.
[17] Wu TR, Zhang XF, Yuan QH, et al. Fast growth of inch-sized single-crystalline graphene from a controlled single nucleus on Cu-Ni alloys. Nat Mater 2016;15:43–7.
[18] Ding D, Solis-Fernandez P, Hibino H, et al. Spatially controlled nucleation of single crystal graphene on Cu assisted by stacked Ni. ACS Nano 2016;10:11196–204.
[19] Vlassiouk IV, Stehle Y, Pudasaini PR, et al. Evolutionary selection growth of two-dimensional materials on polycrystalline substrates. Nat Mater 2018;17:318–22.
[20] Xu XZ, Zhang ZH, Qiu L, et al. Ultrafast growth of single-crystal graphene assisted by a continuous oxygen supply. Nat Nanotechnol 2016;11:930–5.
[21] Wang H, Xu XZ, Li JY, et al. Surface monocrystallization of copper foil for fast growth of large single-crystal graphene under free molecular Flow. Adv Mater 2016;28:8968–74.

[22] Lin L, Sun LZ, Zhang JC, et al. Rapid growth of large single-crystalline graphene via second passivation and multistage carbon supply. Adv Mater 2016;28:4671–7.
[23] Chen W, Zhao J, Zhang J, et al. Oxygen-assisted chemical vapor deposition growth of large single-crystal and high-quality monolayer MoS_2. J Am Chem Soc 2015;137:15632–5.
[24] Guo W, Jing F, Xiao J, et al. Oxidative-etching-assisted synthesis of centimeter-sized single-crystalline graphene. Adv Mater 2016;28:3152–8.
[25] Guo W, Wu B, Wang S, et al. Controlling fundamental fluctuations for reproducible growth of large single-crystal graphene. ACS Nano 2018;12:1778–84.
[26] Yang W, Chen GR, Shi ZW, et al. Epitaxial growth of single-domain graphene on hexagonal boron nitride. Nat Mater 2013;12:792–7.
[27] Lee JH, Lee EK, Joo WJ, et al. Wafer-scale growth of single-crystal monolayer graphene on reusable hydrogen-terminated germanium. Science 2014;344:286–9.
[28] Dai JY, Wang DX, Zhang M, et al. How graphene islands are unidirectionally aligned on the Ge(110) surface. Nano Lett 2016;16:3160–5.
[29] Brown L, Lochocki EB, Avila J, et al. Polycrystalline graphene with single crystalline electronic structure. Nano Lett 2014;14:5706–11.
[30] Nguyen VL, Shin BG, Duong DL, et al. Seamless stitching of graphene domains on polished copper (111) foil. Adv Mater 2015;27:1376–82.
[31] Nguyen VL, Perello DJ, Lee S, et al. Wafer-scale single-crystalline AB-stacked bilayer graphene. Adv Mater 2016;28:8177–83.
[32] Xu XZ, Zhang ZH, Dong JC, et al. Ultrafast epitaxial growth of metre-sized single-crystal graphene on industrial Cu foil. Sci Bull 2017;62:1074–80.
[33] Jin S, Huang M, Kwon Y, et al. Colossal grain growth yields single-crystal metal foils by contact-free annealing. Science 2018;362:1021–5.
[34] Nai CT, Xu H, Tan SJR, et al. Analyzing dirac cone and phonon dispersion in highly oriented nanocrystalline graphene. ACS Nano 2016;10:1681–9.
[35] Gao LB, Xu H, Li LJ, et al. Heteroepitaxial growth of wafer scale highly oriented graphene using inductively coupled plasma chemical vapor deposition. 2D Mater 2016;3:021001.
[36] Hu BS, Ago H, Ito Y, et al. Epitaxial growth of large-area single-layer graphene over Cu(111)/sapphire by atmospheric pressure CVD. Carbon 2012;50:57–65.
[37] Nie S, Wofford JM, Bartelt NC, et al. Origin of the mosaicity in graphene grown on Cu(111). Phys Rev B 2011;84:155425.
[38] Wang XL, Yuan QH, Li J, et al. The transition metal surface dependent methane decomposition in graphene chemical vapor deposition growth. Nanoscale 2017;9:11584–9.
[39] Zhen Z, Li X, Zhu H. Synthesis of two dimensional materials on extremely clean surfaces. Nano Today 2018;22:7–9.
[40] Miller DL, Keller MW, Shaw JM, et al. Epitaxial (111) films of Cu, Ni, and CuxNiy on α-Al_2O_3(0001) for graphene growth by chemical vapor deposition. J Appl Phys 2012;112:1706504.
[41] Takesaki Y, Kawahara K, Hibino H, et al. Highly uniform bilayer graphene on epitaxial Cu-Ni(111) alloy. Chem Mater 2016;28:4583–92.
[42] Ago H, Kawahara K, Ogawa Y, et al. Epitaxial growth and electronic properties of large hexagonal graphene domains on Cu(111) thin film. Appl Phys Express 2013;6:075101.
[43] Lu ZH, Sun X, Xiang Y, et al. Revealing the crystalline integrity of wafer-scale graphene on SiO_2/Si: an azimuthal RHEED approach. ACS Appl Mater Interfaces 2017;9:23081–91.
[44] Oh SH, Scheu C, Wagner T, et al. Epitaxy and bonding of Cu films on oxygen-terminated α-Al_2O_3(0001) surfaces. Acta Mater 2006;54:2685–96.
[45] Deng B, Pang ZQ, Chen SL, et al. Wrinkle-free single-crystal graphene wafer grown on strain-engineered substrates. ACS Nano 2017;11:12337–45.
[46] Han GH, Gunes F, Bae JJ, et al. Influence of copper morphology in forming nucleation seeds for graphene growth. Nano Lett 2011;11:4144–8.
[47] Liu YF, Wu TR, Yin YL, et al. How low nucleation density of graphene on CuNi alloy is achieved. Adv Sci 2018;5:1700961.
[48] Yan Z, Liu YY, Ju L, et al. Large hexagonal bi- and trilayer graphene single crystals with varied interlayer rotations. Angew Chem Int Ed 2014;53:1565–9.
[49] Duong DL, Han GH, Lee SM, et al. Probing graphene grain boundaries with optical microscopy. Nature 2012;490:235.
[50] Yu QK, Jauregui LA, Wu W, et al. Control and characterization of individual grains and grain boundaries in graphene grown by chemical vapour deposition. Nat Mater 2011;10:443–9.
[51] Li XS, Cai WW, Colombo L, et al. Evolution of graphene growth on Ni and Cu by carbon isotope labeling. Nano Lett 2009;9:4268–72.
[52] Overbury SH, Bertrand PA, Somorjai GA. Surface composition of binary systems. Prediction of surface phase diagrams of solid solutions. Chem Rev 1975;75:547–60.
[53] Lewis AM, Derby B, Kinloch IA. Influence of gas phase equilibria on the chemical vapor deposition of graphene. ACS Nano 2013;7:3104–17.
[54] Li G, Huang SH, Li ZY. Gas-phase dynamics in graphene growth by chemical vapour deposition. Phys Chem Chem Phys 2015;17:22832–6.
[55] Blake P, Brimicombe PD, Nair RR, et al. Graphene-based liquid crystal device. Nano Lett 2008;8:1704–8.
[56] Wang HH, Liu BZ, Wang L, et al. Graphene glass inducing multidomain orientations in cholesteric liquid crystal devices toward wide viewing angles. ACS Nano 2018;12:6443–51.
[57] Kim DW, Kim YH, Jeong HS, et al. Direct visualization of large-area graphene domains and boundaries by optical birefringency. Nat Nanotechnol 2012;7:29–34.
[58] Deng B, Hsu PC, Chen GC, et al. Roll-to-roll encapsulation of metal nanowires between graphene and plastic substrate for high-performance flexible transparent electrodes. Nano Lett 2015;15:4206–13.
[59] Chandrashekar BN, Deng B, Smitha AS, et al. Roll-to-roll green transfer of CVD graphene onto plastic for a transparent and flexible triboelectric nanogenerator. Adv Mater 2015;27:5210–6.
[60] Ng RLM, Bredif M, Duval G, et al. Light field photography with a hand-held plenoptic camera. Stanford Tech Rep CSTR 2005;2:11.
[61] Lumsdaine A, Lin LL, Willcock J, et al. Fourier analysis of the focused plenoptic camera. Proc SPIE 2013:8667.
[62] Lei Y, Tong Q, Zhang XY, et al. An electrically tunable plenoptic camera using a liquid crystal microlens array. Rev Sci Instrum 2015;86:053101.
[63] Xin ZW, Wei D, Xie XW, et al. Dual-polarized light-field imaging micro-system via a liquid-crystal microlens array for direct three-dimensional observation. Opt Express 2018;26:4035–49.
[64] Tong Q, Chen M, Xin Z, et al. Depth of field extension and objective space depth measurement based on wavefront imaging. Opt Express 2018;26:18368–85.
[65] Patel JS, Rastani K. Electrically controlled polarization-independent liquid-crystal fresnel lens arrays. Opt Lett 1991;16:532–4.
[66] Tong Q, Lei Y, Xin ZW, et al. Dual-mode photosensitive arrays based on the integration of liquid crystal microlenses and CMOS sensors for obtaining the intensity images and wavefronts of objects. Opt Express 2016;24:1903–23.

Bing Deng received his B.Sc degree in Chemistry from Peking University in 2014. He is currently pursuing a Ph.D. degree at the College of Chemistry and Molecular Engineering, Peking University at Beijing, China under the guidance of Profs. Hailin Peng and Zhongfan Liu. His current research is focused on controlled synthesis of high-quality graphene films by chemical vapor deposition method and the applications in flexible electronics.

Zhongfan Liu received his Ph.D. degree from the University of Tokyo in 1990. After a postdoctoral fellowship at the Institute for Molecular Science, Japan, he became an associate professor (1993), full professor (1993), and Cheung Kong Chair professor (1999) of Peking University. His research interests focus on low-dimensional carbon materials and novel 2D atomic crystals, targeting nanoelectronic and energy conversion devices together with the exploration of fundamental phenomena in nanoscale systems.

Hailin Peng received his B.S. degree in Chemistry from Jilin University in 2000, and his Ph.D. degree in Physical Chemistry from Peking University in 2005. After postdoctoral study in Stanford University during 2005–2009, he became an associate professor (2009) and full professor (2014) of Peking University. Currently, his research interests focus on synthesis of heterostructures and optoelectronic devices of 2D materials such as graphene, nanostructured topological insulators, and other novel 2D crystals.